Journal of
Materials Chemistry C

REVIEW

View Article Online
View Journal | View Issue

Cite this: J. Mater. Chem. C, 2018, 6, 5353

Rational design and synthesis of bifunctional metal nanocrystals for probing catalytic reactions by surface-enhanced Raman scattering

Yun Zhang,[ab] Yiren Wu[a] and Dong Qin *[a]

Received 23rd March 2018,
Accepted 2nd May 2018

DOI: 10.1039/c8tc01394b

rsc.li/materials-c

This report highlights recent progress in the rational design, synthesis, and applications of bimetallic nanocrystals with integrated SERS and catalytic activities. The ultimate goal is to develop bifunctional nanocrystals as a SERS probe for monitoring a catalytic reaction *in situ*. We first introduce seeded growth as a facile and powerful route to the syntheses of bifunctional nanocrystals with catalytic activities arising from Au or Pd, in addition to plasmonic properties originating from Ag or Au. Specifically, we discuss two distinctive pathways, namely conformal and site-selected deposition of a second metal on the surface of a noble-metal nanocrystal seed, for the fabrication of bifunctional nanocrystals with controlled composition and morphology. We then discuss the application of these bifunctional nanocrystals as unique probes for *in situ* SERS monitoring of the Au or Pd-catalyzed reduction of 4-nitrothiophenol to 4-aminothiophenol by $NaBH_4$ and the Ag-catalyzed oxidation of 4-aminothiophenol to *trans*-4,4′-dimercaptoazobenzene by the O_2 from air. We conclude this review with perspectives on the future development.

1. Introduction

Noble-metal nanocrystals with well-defined compositions and shapes (*i.e.*, facets or surface structures) have been extensively explored as heterogeneous catalysts for applications related to organic synthesis,[1–6] energy conversion,[7–12] and degradation of pollutants.[13–16] In order to elucidate the mechanisms involved in the catalytic reactions, it is of crucial importance to detect and monitor the reaction intermediates and products *in situ*. To this end, surface-enhanced Raman scattering (SERS) offers a powerful tool that can be applied for chemical detection with sensitivity down to the single-molecule level.[17–21] In order to realize the potential of SERS as a power tool for *in situ* analysis of a catalytic reaction, it is essential to develop a bifunctional probe that is both plasmonically and catalytically active. Fig. 1A shows a small portion of the periodic table to highlight the elements of interest. It has been well-established that Ag and Au nanocrystals embrace strong localized surface plasmon resonance (LSPR) peaks in the visible and near-infrared regions for SERS detection.[22–26] In principle, Ag or Au nanocrystals and their bimetallic counterparts can readily serve as the bifunctional probe but the reactions catalyzed by these two metals are somewhat limited. In comparison, the platinum-group metals (PGMs) such as Pt and Pd are able to catalyze a much broader range of chemical reactions, but they are extremely poor SERS substrates because of the very weak coupling between their free electrons and the visible or near-infrared light.[27–31] Ideally, one

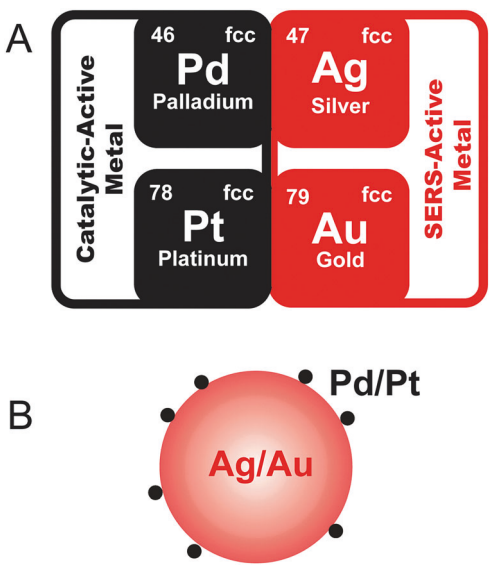

Fig. 1 Schematic illustration showing (A) four noble-metal elements with distinct plasmonic and catalytic properties; and (B) bifunctional nanocrystals by assembling Ag or Au nanocrystals with Pd or Pt nanoparticles.

[a] School of Materials Science and Engineering, Georgia Institute of Technology, Atlanta, Georgia 30332, USA
[b] College of Chemistry and Chemical Engineering, Lanzhou University, Lanzhou, Gansu 730000, P. R. China. E-mail: dong.qin@mse.gatech.edu

can design and fabricate a bifunctional probe by simply taking one metal from each group and having them integrated together in a bimetallic format.

To fabricate a bimetallic system for its potential use as a bifunctional probe, one has to avoid the formation of alloys because the desired plasmonic and catalytic properties may not be presented simultaneously in an alloy. In a sense, the two metals should keep their individual identities in the bimetallic system for attaining the dual functionality. Fig. 1B outlines an easy approach for generating such a bifunctional probe by processing the two metals as nanocrystals separately and then having them mixed and assembled into a bimetallic system.[32] Although the assembly process can be initiated and manipulated by controlling the surface functional groups (including charges) on the nanocrystals, the final products tend to be poorly controlled in terms of composition, size, shape, and structure. In particular, the presence of organic molecules between adjacent metal nanocrystals may hinder the electronic coupling between two metal surfaces, compromising their utility as a dual-functional probe.

There are three general strategies that have been documented for the syntheses of bimetallic nanocrystals. Coreduction is a simple and versatile approach that relies on the concurrent reduction of two metal precursors to generate two types of atoms for their nucleation and growth into nanocrystals of alloys.[33] Galvanic replacement reaction relies on the oxidation of one metal from the template for the reduction of the precursor of another metal to generate atoms followed by their deposition on the template.[34] Seeded growth offers one of the most effective routes to the facile synthesis of bimetallic nanocrystals by using the preformed nanocrystals as ''seeds'' to direct and dictate the deposition of the second metal.[35–38] Specifically, when a precursor to the second metal is introduced into a mixture containing the seeds, reducing agent, capping agent, and colloidal stabilizer, it will be reduced to zero-valent atoms, which then heterogeneously nucleate and grow from the surface of the seeds to generate bimetallic nanocrystals. By carefully choosing a proper combination of seeds, metal precursor, and other experimental conditions, one can obtain bimetallic nanocrystals with well-defined compositions, sizes, shapes, and structures to meet the requests of different applications.[39–43] In general, the second metal can be deposited on the seed conformally or in a site-selected fashion. When conformal deposition is involved, the seed is typically made of a plasmonic metal while the catalytic activity will be provided by the second metal. For site-selected deposition, however, one can even generate a dual catalyst by exploring the catalytic properties exhibited by both the seed and the second metal.

This review provides a short overview of recent advances related to the design, synthesis, and applications of a novel class of bimetallic nanocrystals with integrated SERS and catalytic activities. We start with a brief introduction to various synthetic protocols that rely on surface capping and kinetic control to tailor the structures of bimetallic nanocrystals. We then discuss two completely different patterns of deposition, namely conformal and site-selected, that are commonly involved in seeded growth, with a focus on the underlying mechanisms. Finally, we present several examples to highlight the use of these nanocrystals as a bifunctional probe for *in situ* monitoring and analyzing catalytic reactions by SERS. The goal of this review is to illustrate how bimetallic nanocrystals can be rationally designed and synthesized with integrated SERS and catalytic activities to serve as novel probes for elucidating the complex mechanisms of catalytic reactions.

2. Synthesis of bifunctional nanocrystals *via* seeded growth

Seeded growth represents one of the most effective routes to the preparation of bimetallic nanocrystals. A number of experimental parameters have been identified for controlling the deposition patterns and thus the outcomes of a synthesis, including the surface energy landscape of the seed (defined by the nature of the metal, the initial size and shape, and the capping agent on the surface) and the interaction between thermodynamic and kinetic parameters involved in a synthesis. With respect to the development of bifunctional probes, Fig. 2 illustrates two strategies for generating bimetallic nanocrystals with desired and tunable properties for specific applications. The first strategy relies on the conformal deposition of a catalytically active element such as Au on the surface of a seed made of a plasmonically active element such as Ag. We use two different examples to illustrate the concept: (i) Ag@Au core–shell nanocubes with an ultrathin (<2 nm) shell to avoid screening the LSPR/SERS properties of the core; and (ii) Ag@Au core–shell concave nanocrystals with sharp edges to further augment the SERS activity. The second strategy leverages the site-selected nucleation and growth for depositing a second metal on the surface of a seed made of Au, Ag or Pd. We select four representative cases to demonstrate the concept: (i) Au@AuPd core–shell nanorods with a Au–Pd alloy deposited as horns at the ends. (ii) Ag@Ag–Pd core–frame nanocubes with the Ag–Pd alloy deposited at the corners and edges only; (iii) Ag@SiO_2/Au nanoparticles with an ''islands in the sea'' configuration; and (iv) Pd–Ag dimeric nanocubes. All these bimetallic nanocrystals show unique integration of LSPR/SERS and catalytic properties for their use as a dual probe in monitoring and analyzing catalytic reactions by SERS.

2.1 Conformal deposition of the second metal on the seed

Ag@Au core–shell nanocubes with an ultrathin Au shell. Fig. 3A shows a schematic diagram for the synthesis of Ag@Au nanocubes through conformal deposition of an ultrathin Au layer on the surface of Ag nanocubes *via* seeded growth.[44,45] The Ag@Au core–shell nanocubes preserves the LSPR properties of Ag, together with enhanced chemical stability. In a typical synthesis, aqueous $HAuCl_4$ was titrated into an aqueous suspension of Ag nanocubes in the presence of ascorbic acid (H_2Asc, a reducing agent), poly(vinylpyrrolidone) (PVP, a stabilizer), and NaOH (a pH modifier) at an initial pH of 11.9 using a syringe pump. It has been argued that the first few droplets of added $HAuCl_4$ would

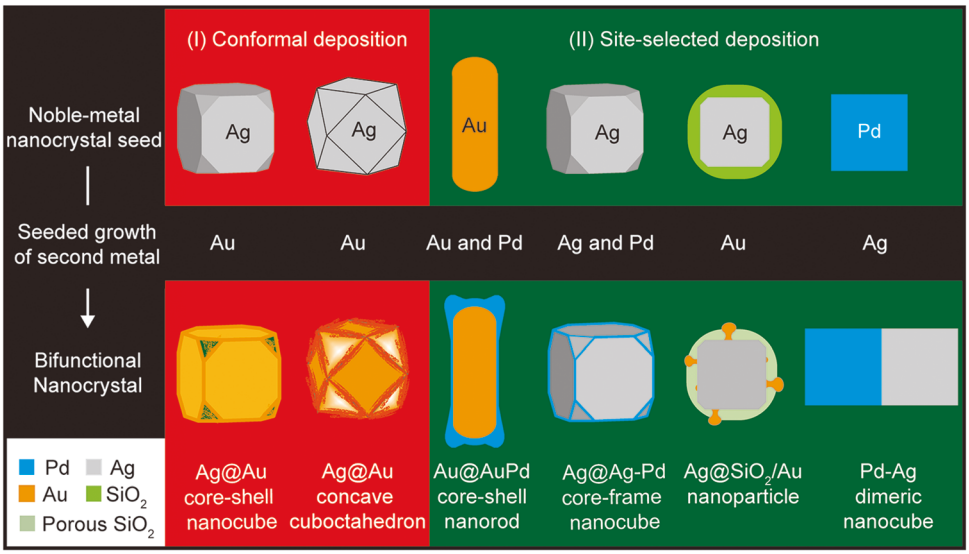

Fig. 2 Schematic illustration showing two different pathways for the deposition of one metal on the surface of a seed made of another metal for the generation of bifunctional nanocrystals with integrated plasmonic and catalytic properties.

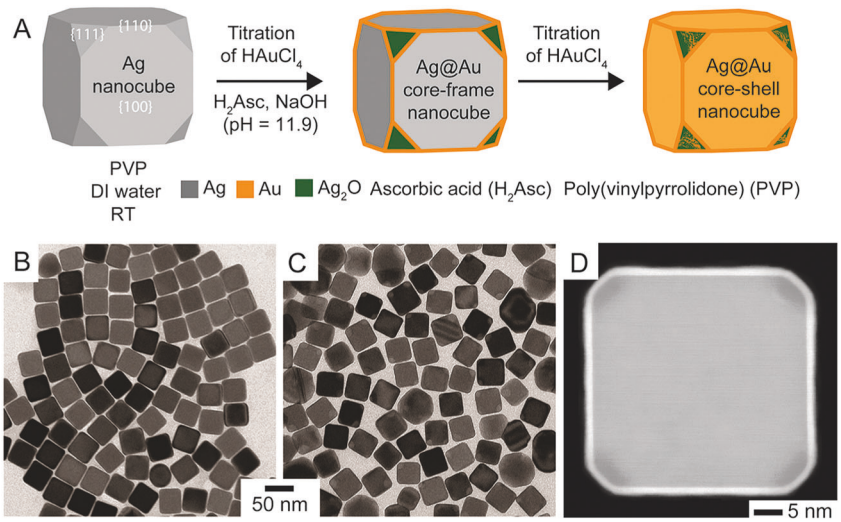

Fig. 3 (A) Schematic illustration of seeded growth of Au on Ag nanocubes by the titration of $HAuCl_4$ solution into a suspension of Ag nanocubes in the presence of H_2Asc, NaOH, and PVP at pH = 11.9. (B and C) TEM images of the Ag nanocubes and Ag@Au core–shell nanocubes. (D) HAADF-STEM image of a core–shell individual nanocube in (C). Reprint with permission from ref. 44, Copyright 2014 American Chemical Society.

react with Ag atoms located on the {111} facets (or corners) of the nanocubes for the initial deposition of Au on the {110} facets (or edges) of nanocubes *via* a galvanic replacement reaction. Concurrently, the released Ag^+ ions would react with OH^- ions instantaneously under an alkaline condition, leading to the formation of Ag_2O patches at the corners. At this time point, the Ag_2O would prevent the underlying Ag from participating in the galvanic reaction anymore, and thus the added $HAuCl_4$ would undergo ligand exchange with OH^- to form $AuCl(OH)_3^-$ and $Au(OH)_4^-$ with decreased reduction potentials relative to that of $AuCl_4^-$. Under this circumstance, these newly formed Au precursors would be reduced by ascorbate monoanion ($HAsc^-$) to generate Au atoms, followed by their deposition onto the entire surface of Ag nanocubes, leading to the formation of Ag@Au core–shell nanocubes. Fig. 3B and C shows TEM images of the Ag nanocubes and Ag@Au nanocubes, indicating that the cubic shape was well preserved. When the nanocube was oriented along the [001] zone axis, Fig. 3D shows an aberration-corrected high-angle annular dark-field scanning TEM (HAADF-STEM) image of the Ag@Au nanocube. An ultrathin layer of Au shell on Ag core can be elucidated from the contrast because of the difference in atomic number between Au and Ag.

Ag@Au concave nanocrystals. Using the same protocol for the synthesis of Ag@Au core–shell nanocubes, Fig. 4 shows the proposed pathway responsible for the transformation of Ag cuboctahedra enclosed by a mixture of {111} and {100} facets at a ratio of 1 : 1.7 in terms of surface area into Ag@Au concave cuboctahedra.[46] In the first step, Au atoms derived from the

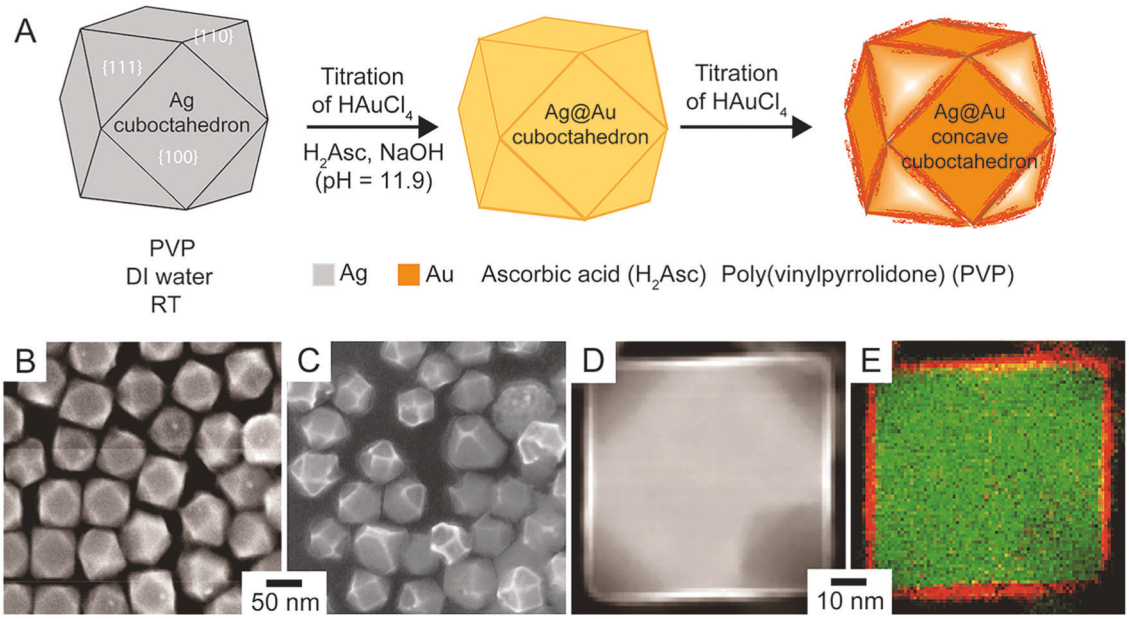

Fig. 4 (A) Schematic illustration of a pathway proposed to account for the deposition of Au on Ag cuboctahedra for the generation of Ag@Au concave cuboctahedra. (B and C) SEM images of the Ag cuboctahedra and Ag@Au concave cuboctahedra. (D and E) HAADF-STEM image of a cuboctahedron shown in (C) and the corresponding STEM-EELS mapping of the same cuboctahedron when it was oriented along the [100] zone axis (red, Au; green, Ag). Reprint with permission from ref. 46, Copyright 2016 American Chemical Society.

reduction by $HAsc^-$ are deposited onto the entire surface of a Ag cuboctahedron to generate a Ag@Au cuboctahedron with a complete thin Au shell. Next, Au atoms will be preferentially deposited on the Au{100} facets due to the selective passivation of Au{111} facets by PVP in an aqueous system, resulting in the formation of a Ag@Au concave cuboctahedron. The concave nanocrystals embrace excellent SERS activity due to the presence of concavity for creating SERS hot spots. On the other hand, the Au atoms deposited on the high-energy index facets can serve as the catalytic sites. Fig. 4B and C shows SEM images of the Ag cuboctahedra and Ag@Au concave cuboctahedra. Fig. 4D gives the HAADF image taken from an individual concave cuboctahedron shown in Fig. 4C with the nanoparticle being aligned with the [100] zone axis. This result clearly indicates the formation of a complete Au shell around the Ag core. Additionally, Fig. 4E shows the distributions of Ag and Au by characterizing the same particle using STEM-electron energy-loss spectroscopy (STEM-EELS), further confirming the uniform deposition of Au on the {100} facets.

2.2 Site-selected deposition of the second metal on the seed

Site-selected deposition is another pattern commonly observed during the seeded growth of metal nanocrystals. In general, the atoms tend to be deposited on the surface of a seed at locations that have low coordination numbers and thus high surface energies or on regions that are not passivated by capping agents. In either case, it will result in growth from selected sites only, rather than the entire surface of a seed in a conformal fashion.

Au@AuPd core–shell nanorods. Fig. 5A shows a schematic illustration of the synthesis of Au@AuPd nanorods through initial deposition of Au–Pd alloy horns on the ends of Au nanorods *via* seeded growth in the setting of co-reduction.[47] In a typical synthesis, $HAuCl_4$ and Na_2PdCl_4 (precursors to Au and Pd, respectively) were co-titrated into a solution containing Au nanorods over a certain period of time. Initially, Au–Pd alloy were selectively deposited on the two ends of each nanorod because the low-coordination sites are more favorable in terms of surface energy for heterogeneous nucleation. As the deposition continued, the horns were generated at the ends of nanorods, followed by the formation of a conformal layer of Au–Pd on the entire surface of the nanorods. Fig. 5B and C shows TEM images of the Au nanorods and as-prepared Au@AuPd nanorods, suggesting that the rod-shape remained. Fig. 5D shows a SEM image of the product, confirming that the newly grown "horns" were positioned at the ends and there were four horns at each end of the nanorod. Fig. 5E shows EDX mapping along different directions, demonstrating that the four {100} lateral faces of the Au nanorod were covered by Au–Pd alloy, but in an ultrathin overlayer comprised of uniformly distributed Pd and Au. The ultrathin overlayer was likely formed through surface diffusion from the atoms initially deposited at the ends. When compared with pure Pd, the Au–Pd alloy grown on the Au nanorods will have a smaller imaginary part of their dielectric constant throughout the visible and near-infrared regime to render a weaker damping effect on their plasmonic property. Nevertheless, these Au@AuPd nanorods show exotic crystal morphologies with high-index facets and thus superior catalytic activity, in addition to the SERS activity.

Ag@Pd–Ag core–frame nanocubes. In contrast to the deposition of Pd on Au nanocrystals, the use of Ag nanocrystals as seeds for the deposition of Pd remained challenging because of the galvanic replacement reaction between Ag and a salt precursor to Pd.

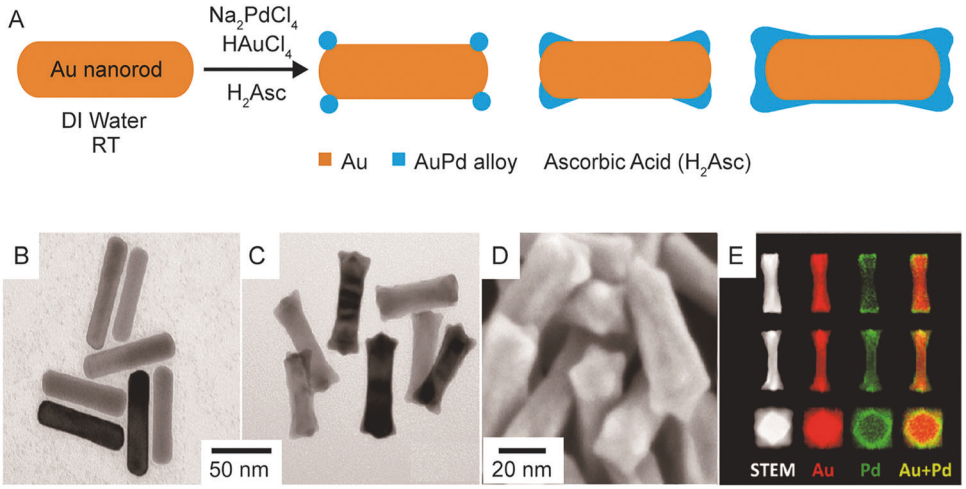

Fig. 5 (A) Schematic illustration deciphering the overgrowth of AuPd alloy on Au nanorod seeds. (B and C) TEM images of the Au nanorods and as-obtained Au@AuPd nanorods. (D) SEM image of the as-obtained Au@AuPd nanorods. (E) HAADF-STEM image and EDX mapping of the Au@AuPd nanorods shown in (C) taken along the [100], [110], and [001] axes, respectively. Reprint with permission from ref. 47, Copyright 2013 American Chemical Society.

Although the replacement reaction allows for the formation of Ag–Pd bimetallic hollow nanostructures with the catalytic properties associated with Pd atoms,[34] the significant loss of Ag content during galvanic replacement often leads to deterioration in SERS activity. Recently, we demonstrated a strategy based on the co-reduction of Ag and Pd precursors for pushing back the galvanic replacement reaction, ultimately generating bimetallic nanocrystals with strong SERS and catalytic activities.[48,49] In one example, we demonstrated the co-deposition of Ag and Pd atoms onto the surface of Ag nanocubes for the generation of Ag@Pd–Ag nanocubes with integrated SERS and catalytic functions.[48] Although the deposition of Pd would dampen and even diminish the SERS activity of the Ag seeds, co-reduction of Pd with Ag could provide a solution to minimize the damping effect, allowing for the retention of the SERS activity.

As schematically illustrated in Fig. 6A, Ag nanocubes (the seed, see Fig. 6B) were dispersed in an aqueous solution containing H_2Asc (the reductant) and PVP (the capping agent and colloidal stabilizer), followed by the co-titration of Na_2PdCl_4 and $AgNO_3$ solutions under ambient conditions using a syringe pump.[48] It was found that the galvanic replacement reaction between Ag nanocubes and Na_2PdCl_4 could be effectively suppressed because of the involvement of Ag^+ ions and H_2Asc, leading to the co-deposition of Ag and Pd atoms onto the surface of the Ag nanocubes. As the volume of the co-titrated precursor solutions was increased, Ag and Pd atoms were progressively deposited on the edges, corners, and side faces of the nanocubes. Fig. 6C shows a TEM image of the products obtained at a co-titration volume of 0.2 mL for each precursor. The corners and edges of the nanocubes were

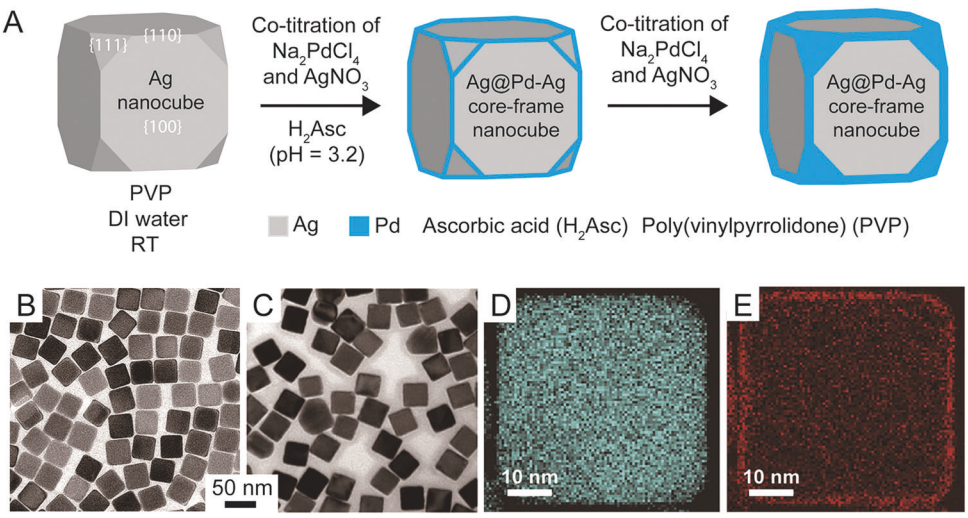

Fig. 6 (A) Schematic illustration showing the overgrowth of Pd and Ag on Ag nanocube seeds through the co-reduction of Na_2PdCl_4 and $AgNO_3$ in the presence of H_2Asc and PVP. (B and C) TEM images of the Ag nanocubes and as-prepared Ag@Pd–Ag nanocubes. (D and E) EDX mapping of Ag and Pd of a Ag@Pd–Ag nanocube shown in (C). Reprint with permission from ref. 48, Copyright 2015 American Chemical Society.

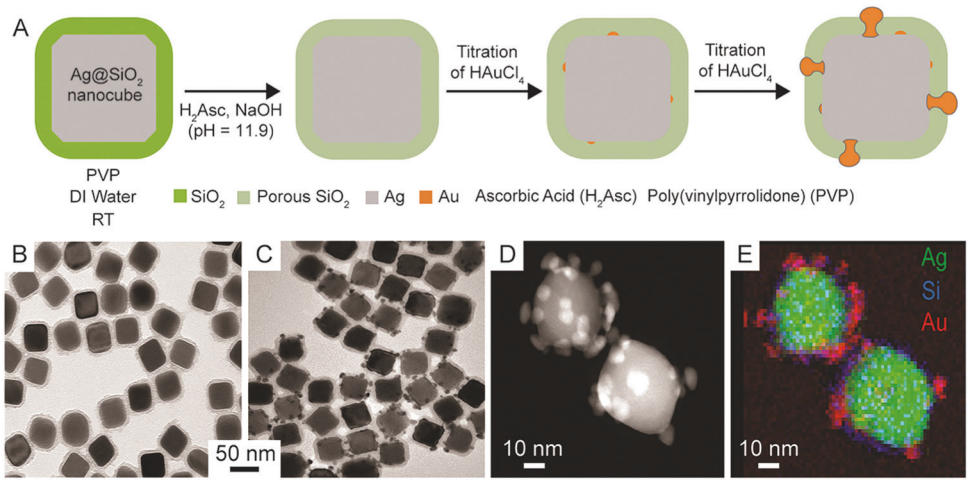

Fig. 7 (A) Schematic illustration showing the deposition of Au islands on Ag@SiO_2 seeds in the presence of H_2Asc, PVP, and NaOH. (B and C) TEM images of the Ag@SiO_2 nanocubes and as-obtained Ag@SiO_2/Au nanoparticles. (D and E) HAADF-STEM image and EELS mapping of two Ag@SiO_2/Au nanoparticles shown in (C). Reprint with permission from ref. 50, Copyright 2017 Wiley-VCH Verlag GmbH & Co.

sharpened, implying the preferential deposition of Ag and Pd atoms at these sites. EDX mapping of an individual nanocube (Fig. 6D and E) confirmed that the Pd atoms were preferentially deposited at the edge and corner sites, leading to the formation of a core–frame structure. The deposition pattern can be attributed to the fact that the {100} facets of a Ag nanocube were selectively passivated by PVP, so the surface free energies of the three low-index facets increased in the order of $\gamma_{100} < \gamma_{111} < \gamma_{110}$. As a result, the Ag and Pd atoms derived from the co-reduction of their precursors were initially deposited on the {110} facets of a Ag nanocube before accessing other sites.

Ag@SiO_2/Au nanoparticles with an "islands in the sea" configuration. Fig. 7A shows another approach that relies on the creation of holes in silica layer for the deposition of Au on Ag@SiO_2 nanocubes in the site-selected manner.[50] In a typical process, we extended the same protocol used for the conformal deposition of Au on Ag nanocubes except for replacing the Ag seeds with Ag@SiO_2 core–shell nanocubes as shown in Fig. 7B. Due to the presence of NaOH in the reaction solution, the thin shell of SiO_2 layer can be etched for the generation of small pores for reagents to access the surface of the Ag nanocube, followed by site-selected deposition of Au atoms through the pores. At early stage, the galvanic replacement reaction between Au precursor and Ag would initiate the nucleation and deposition of Au atoms on the surface of Ag nanocubes. As the titration is continued, the pores within the SiO_2 shell are gradually filled by the Au atoms derived from the chemical reduction by H_2Asc, leading to the generation of Ag@SiO_2/Au nanoparticles with isolated, well-defined Au islands immersed in a sea made of SiO_2. Fig. 7C shows a TEM image of the as-obtained sample, indicating the formation of Au islands over the surface of each Ag@SiO_2 nanocube. Fig. 7D shows a HAADF-STEM image of two Ag@SiO_2/Au nanoparticles, from which Au could be distinguished from Ag by contrast. The electron energy-loss spectroscopy (EELS) mapping of these two nanoparticles further confirmed the generation of individual Au nanoparticles on the surface of each Ag nanocube while SiO_2 serves as a spacer among the islands.

Pd–Ag dimeric nanocubes. In addition to depositing the catalytic active Pd on the seeds of plasmonically active Ag nanocrystals, one can selectively deposit Ag on Pd nanocrystal seeds to attain bifunctional nanocrystals.[51] In this case, however, it is essential to direct an asymmetric growth to avoid screening the catalytic activity of Pd by the conformal layer of Ag. Fig. 8A shows a schematic illustration to induce site-selected deposition of Ag on a Pd nanocube by manipulating the reduction kinetics. In a typical process, Pd nanocubes with an average length of 16 nm (see Fig. 8B) were dispersed in an aqueous solution of H_2Asc and PVP, followed by the injection of aqueous $AgNO_3$. In principle, the injection rate of $AgNO_3$ solution determines the reduction rate, and ultimately the instantaneous number of the Ag atoms derived from the chemical reduction. At a slower injection rate of 1 mL h^{-1}, the small number of Ag atoms could only lead to nucleation on one of the six side faces of a Pd cubic seed, resulting in asymmetric growth of Ag on Pd for the generation of Pd–Ag dimmers (Fig. 8C). In comparison, at a moderate injection rate of 30 mL h^{-1}, the Ag atoms would nucleate and grow on three adjacent side faces of a Pd cubic seed for the generation of an eccentric, hybrid cube (Fig. 8D). Remarkably, such asymmetric growth of plasmonic metal on the catalytic seeds embraces great potential to fabricate bifunctional nanocrystals with both catalytic and SERS activities.

3. Bifunctional nanocrystals for probing catalytic reactions by SERS

In principle, one can apply the bifunctional nanocrystals described in Section 2 to investigate any chemical reaction that is catalyzed by Ag, Au, and Pd. In literature, however, the reduction of 4-nitrothiophenol (4-NTP) and the subsequent oxidation of 4-aminothiophenol (4-ATP) have been used as two

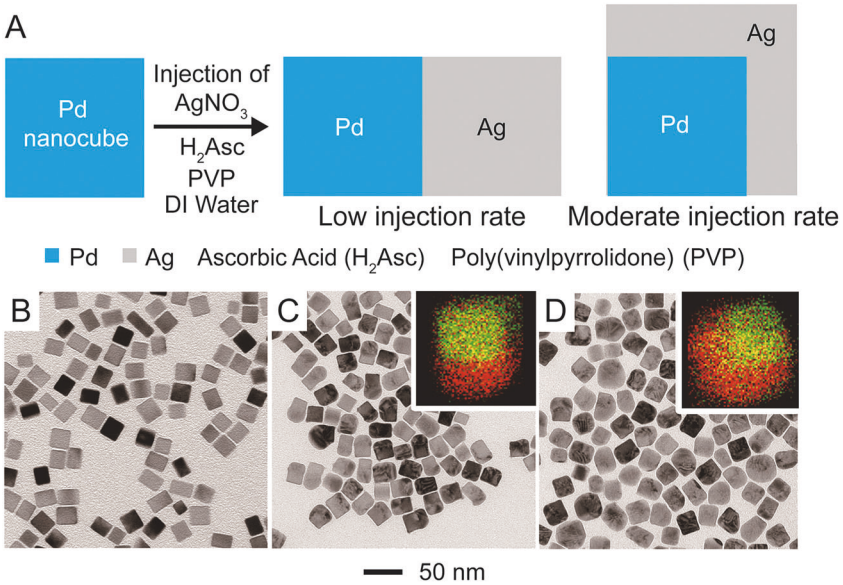

Fig. 8 (A) Schematic illustration showing the deposition of Ag on 18 nm Pd nanocube seeds in the presence of H_2Asc and PVP. TEM images of Pd nanocubes before (B) and after reaction with $AgNO_3$ by controlling the injection rate at (C) 1 mL h^{-1} and (D) 30 mL h^{-1}, respectively. Insets: EDX mapping (green, Pd; red, Ag) of individual nanocrystals shown in figure (C) and (D), respectively. Reprint with permission from ref. 51, Copyright 2012 Wiley-VCH Verlag GmbH & Co.

model reactions for such studies because of the strong SERS signals from these two molecular species and their well-assigned peak positions, in addition to the easiness of carrying out such experiments, including *in situ* measurements.[52–56] Under carefully controlled conditions, even the reaction intermediate, such as 4,4-dimercaptoazobenzene (DMAB), can also be detected and monitored as a function of reaction time.

3.1 Ag–Au bimetallic nanocrystals

By combining the outstanding SERS activity associated with the sharpened corners and edges of concave cuboctahedra with the catalytic activity of Au atoms on the surface, we have demonstrated the use of Ag@Au concave cuboctahedra as a distinctive probe for monitoring the reduction of 4-NTP by $NaBH_4$ *in situ*.[46] We collected time-dependent SERS spectra from an aqueous suspension of the 4-NTP functionalized concave cuboctahedra upon the introduction of $NaBH_4$ (Fig. 9A) at excitation wavelength of 785 nm. At t = 0 min, the SERS spectrum of 4-NTP showed three characteristic peaks located at 1108 cm^{-1} (ν_{CN}), 1336 cm^{-1} (ν_{NO_2}), and 1572 cm^{-1} (ν_{CC}), respectively. The peak located at 1083 cm^{-1} can be assigned to the ν_{CS} band. At t = 6 min, four new bands appeared in the spectrum as the intensities of three peaks associated with 4-NTP decreased. Among those, the peak situated at 1595 cm^{-1} can be assigned to the ν_{CC} of 4-ATP while the other three peaks at 1142 cm^{-1} ($\beta_{CH} + \nu_{CN}$), 1388 cm^{-1} ($\nu\nu_{NN} + \nu_{CN}$), and 1429 cm^{-1} ($\nu_{NN} + \beta_{CH}$) can be assigned to *trans*-DMAB, respectively. From 14 to 17 min, all the peaks of 4-NTP and the three bands of *trans*-DMAB gradually disappeared while the ν_{CC} of 4-ATP increased continuously. At t = 19 min, all three peaks can be signed to 4-ATP, indicating the complete reduction of 4-NTP to 4-ATP. Fig. 9B outlines a proposed mechanism to illustrate the reaction of 4-NTP by $NaBH_4$ on the surface of the Ag@Au concave cuboctahedra. We argue that the first step involves the reduction of the N–O bonds for the generation of nitro- and hydroxylamine, followed by the condensation of these two intermediates to generate *trans*-DMAB. Next, the hydrogenation results in the cleavage of the azo bond toward the production of 4-ATP. Because *trans*-DMAB was detected as an intermediate before the formation of 4-ATP as the final product by SERS, we believe that the reaction of 4-NTP catalyzed by Au is rather slow. Taken together, the Ag@Au concave cuboctahedra can indeed serve as a dual-functional probe for *in situ* monitoring of Au-catalyzed reactions.

The Ag@SiO_2/Au nanoparticle with an ''islands in the sea'' configuration can also serve as a dual-functional probe to catalyze and monitor the reaction simultaneously.[50] Fig. 9C shows a series of SERS spectra collected from an aqueous suspension of the 4-NTP functionalized Ag@SiO_2/Au nanoparticles upon the introduction of $NaBH_4$ at the excitation wavelength of 532 nm. At t = 0 min, the SERS spectrum shows three signature bands of 4-NTP at 1109, 1338, and 1572 cm^{-1}. At t = 9 min, the intensities of 4-NTP bands decreased drastically. By t = 22 min, the three bands of 4-NTP disappeared while a small peak of 4-ATP appeared at 1594 cm^{-1}, indicating the completion of reduction of 4-NTP to 4-ATP. From 22 to 66 min, the SERS spectra remained unchanged. At t = 89 min, four peaks associated with *trans*-DMAB appeared at 1142, 1387, 1429, and 1574 cm^{-1}, indicating the oxidation of 4-ATP to *trans*-DMAB by the O_2 from air. At t = 120 min, the spectrum remained essentially the same except for a slight increase in intensity for the peaks. Fig. 9D illustrates the mechanistic details proposed to account for the reduction of 4-NTP by $NaBH_4$ when Ag@SiO_2/Au nanoparticles are used as a catalyst. In the first step, the Au islands could serve

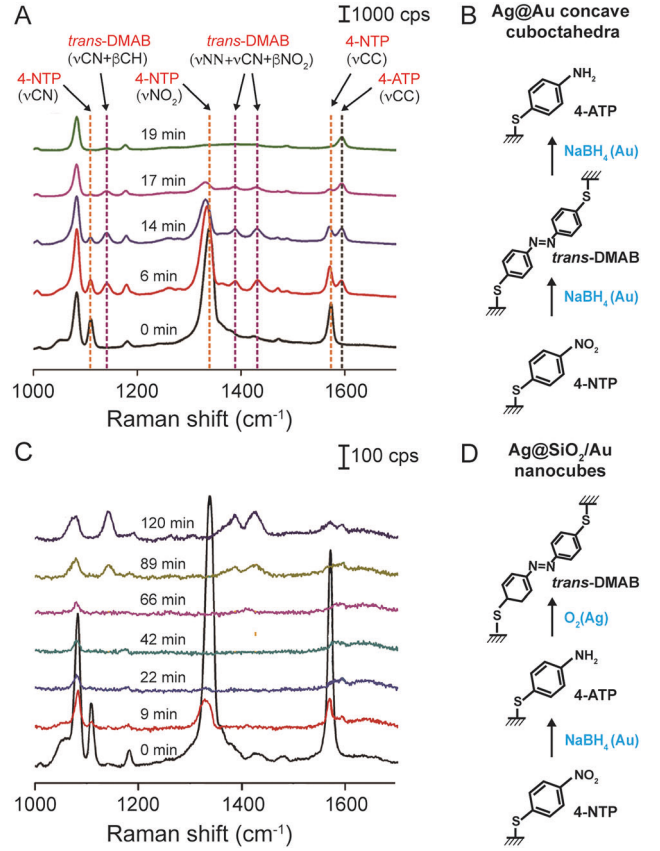

Fig. 9 (A) Time-dependent SERS spectra for monitoring the reduction of 4-NTP by $NaBH_4$ using Ag@Au concave cuboctahedra as catalysts. (B) The proposed reaction pathway for the reduction of 4-NTP by $NaBH_4$ with Ag@Au concave cuboctahedra. (C) Time-dependent SERS spectra for monitoring the reduction of 4-NTP by $NaBH_4$ using $Ag@SiO_2/Au$ as catalysts. (D) The proposed reaction pathway involved in the reduction of 4-NTP by $NaBH_4$ with $Ag@SiO_2/Au$ nanocubes. Reprint with permission from ref. 46 and 50. Copyright 2016 American Chemical Society and 2017 Wiley-VCH Verlag GmbH & Co.

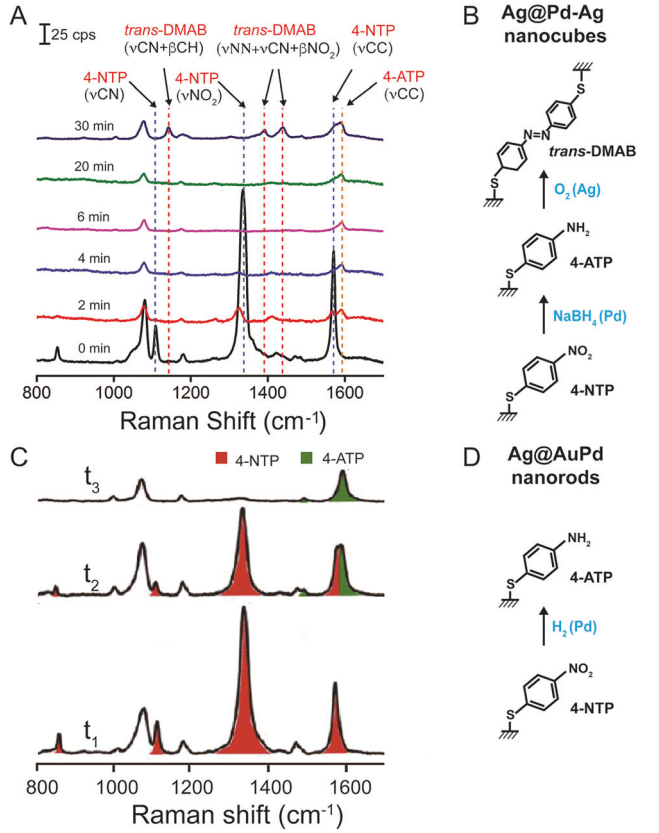

Fig. 10 (A) Time-dependent SERS spectra for monitoring the reduction of 4-NTP by $NaBH_4$ using Ag@Pd–Ag nanocubes as catalysts. (B) The proposed reaction pathway for the reduction of 4-NTP by $NaBH_4$ with Ag@Pd–Ag nanocubes. (C) Time-dependent SERS spectra for monitoring the reduction of 4-NTP by $NaBH_4$ using Au@AuPd nanorods as catalysts (at the different reaction stage, $t_1 < t_2 < t_3$). (D) The proposed reaction pathway involved in the reduction of 4-NTP by $NaBH_4$ with Au@AuPd nanorods. Reprint with permission from ref. 49 and 47, Copyright 2016 Wiley-VCH Verlag GmbH & Co. and 2013 American Chemical Society.

as a catalyst to facilitate the reduction of 4-NTP to 4-ATP by $NaBH_4$. In this case, we did not observe the formation of *trans*-DMAB from the SERS spectra, suggesting that the reduction rate was faster. It is also possible that the SERS signal of *trans*-DMAB is too weak to be observed. Once $NaBH_4$ was completely consumed in the reaction solution, the Ag atoms could activate the O_2 dissolved in the solution for the oxidation of 4-ATP to *trans*-DMAB. Collectively, $Ag@SiO_2/Au$ nanoparticles can serve as a dual-functional probe for monitoring the Au-catalyzed reduction of 4-NTP by $NaBH_4$ *in situ* and subsequently the Ag-catalyzed oxidation of 4-ATP by the O_2 from air. This data is completely different from of Ag@Au concave cuboctahedra with which H_2O_2 was needed to convert 4-ATP to *trans*-DMAB.[46]

3.2 Ag–Pd and Au–Pd bimetallic nanocrystals

The Ag@Pd–Ag core–frame nanocubes prepared with 4.6 wt% of Pd on the surface could serve as an active SERS substrate and a dual catalyst toward both reduction and oxidation reactions.[49] In this case, the Pd and Ag atoms were mainly deposited on the edge and corner sites of each Ag nanocube, leaving the side faces covered by the Ag atoms of the original nanocube. Fig. 10A shows the time-dependent SERS spectra recorded from an aqueous suspension of the 4-NTP-functionalized core–frame nanocubes before and after the introduction of $NaBH_4$ at the excitation wavelength of 532 nm. At t = 0 min, the spectrum shows three vibrational bands of 4-NTP at 1108, 1336, and 1572 cm^{-1}. At t = 2 min, all the three bands of 4-NTP began to decrease in intensity and a new peak with its assignment to the ν_{CC} of 4-ATP appeared at 1595 cm^{-1}. As the reaction continued to 4 min, only the bands of 4-ATP were resolved, suggesting the complete conversion of 4-NTP to 4-ATP. During the period of 6–20 min, the spectra remained essentially the same. At t = 30 min, three new peaks at 1142, 1388, and 1429 cm^{-1} appeared, with their assignment to *trans*-DMAB. This observation indicates that the 4-ATP adsorbed on the surface of the Ag@Pd–Ag nanocubes could be oxidized by the O_2 from air to generate *trans*-DMAB once the reduction of 4-NTP had been completed and all the residual $NaBH_4$ in the solution had decomposed. Fig. 10B shows a proposed reaction mechanism account for the production of *trans*-DMAB by the reduction of

4-NTP by $NaBH_4$. The first step involved the Pd-catalyzed reduction of 4-NTP to 4-ATP by the H_2 from $NaBH_4$ without the detection of *trans*-DMAB. This is different from the Au-catalyzed reduction as discussed in Section 3.1. Next, the 4-ATP molecules derived from 4-NTP could retain their identity without undergoing any changes as long as there was residual $NaBH_4$ in the reaction solution. Finally, upon the complete decomposition of $NaBH_4$, the 4-ATP was quickly transformed to *trans*-DMAB by the O_2 from air as catalyzed by Ag atoms on the side faces. Collectively, this work demonstrated the use of Ag@Pd–Ag core–frame nanocubes as a dual catalyst for both reduction and oxidation reactions and, at the same time, as an active SERS probe for monitoring both the reactions under ambient conditions.

In an independent study, the bifunctional Au@AuPd nanorods shown in Fig. 5 were also demonstrated as a SERS probe for monitoring a catalytic reaction *in situ*.[47] The rod-like morphology of the particles yielded a strong LSPR, with electric field localized at the ends that were enclosed by high-index facets and could thus serve as highly active sites for catalytic reactions. The AuPd alloy horns at the ends not only enhanced the catalytic activity but also helped circumvent plasmonic damping to a great extent. Fig. 10C demonstrates the capability to simultaneously catalyze and monitor the hydrogenation of 4-NTP to 4-ATP using the Au@AuPd nanorods at room temperature. Specifically, 4-NTP molecules were immobilized as a monolayer on the surface of the nanorods through chemisorption and then reduced to 4-ATP upon the introduction of a hydrogen flow, as catalyzed by Pd. At the early stage (t_1), the SERS spectrum of the 4-NTP exhibited characteristic bands at 1109, 1334, and 1571 cm^{-1}. Next (t_2), the intensities of the 4-NTP bands dropped while the new characteristic peak of 4-ATP at 1587 cm^{-1} emerged, indicating the conversion of 4-NTP to 4-ATP. At the final stage (t_3), only the peak of 4-ATP was observed, indicating the complete reduction of 4-NTP to 4-ATP. Fig. 10D shows a schematic illustration of the mechanism for the reduction of 4-NTP to 4-ATP by H_2 on the surface of Au@AuPd nanorods. No *trans*-DMAB was detected as an intermediate before the formation of 4-ATP, nor as a final product, indicating that the reduction of 4-NTP follow a direct pathway, which is similar to the case of Ag@Pd–Ag core–frame nanocubes. However, no oxidation of 4-ATP to *trans*-DMAB was observed in the case of Au@AuPd nanorods because Au could not enable the activation of O_2 dissolved in the reaction solution for the oxidation of 4-ATP to *trans*-DMAB as done by Ag. Collectively, these studies clearly demonstrate that metals with catalytic and plasmonic properties can be integrated together to generate bifunctional nanocrystals capable of concurrently catalyzing and monitoring chemical reactions *in situ* by SERS.

4. Conclusions and outlook

We have discussed the recent progress in the rational design, synthesis, and applications of a new class of bimetallic nanocrystals with integrated SERS and catalytic activities for monitoring catalytic reactions *in situ*. We start with an introduction to seeded growth, a prevailing method for controlling the deposition of one metal on the surface of seeds made of another metal and thus generating bimetallic nanocrystals with two different configurations. To this end, conformal deposition of Au on Ag nanocubes or cuboctahedra results in the generation of Ag@Au core–shell nanocubes and Ag@Au concave cuboctahedra. On the other hand, site-selected deposition of Pd on Au nanorods and Ag nanocubes, Au on $Ag@SiO_2$ nanocubes, or Ag on Pd nanocubes leads to the production of a number of bimetallic nanostructures with integrated plasmonic and catalytic properties. With the hydrogenation of 4-NTP as a model system, these bifunctional nanocrystals have been applied as a dual probe to monitor catalytic reactions *in situ* by SERS. It was demonstrated that both Au and Pd could effectively catalyze the reduction of 4-NTP to 4-ATP while Ag could further catalyze the oxidation of 4-ATP to *trans*-DMAB. These bifunctional nanocrystals not only illustrate how bimetallic nanocrystals with integrated SERS and catalytic properties can be rationally designed and synthesized but also provide a novel class of probes for elucidating the complex mechanisms of catalytic reactions. The results demonstrate the new ubiquity of SERS that leverages the bifunctional probes to characterize the reaction intermediates and products by vibrational spectroscopy *in situ*, making it possible to monitor the dynamic processes of catalysis. Moving forward, the ability to deposit catalytically significant element to Ag and Au nanocrystals would expand the utility of SERS to these non-SERS active catalytic materials such as Pd, Pt, Rh, Ir, and Ru for the study of catalytic reactions. Although it remains challenging to study a variety of chemical reactions when the ligands can't bind to the surfaces strongly, *in situ* vibrational spectroscopy with the sensitivity of single molecule detection opens up the possibility to explore the structure and property relationship for metal-catalyzed reactions, and ultimately, address some unresolved issues in heterogeneous catalysis.

Conflicts of interest

There are no conflicts to declare.

Acknowledgements

We acknowledge the support from the National Science Foundation (CHE-1708300), start-up funds from the Georgia Institute of Technology (GT), and a 3M non-tenured faculty award. Y. Z. acknowledges the International Postdoctoral Exchange Fellowship from the China Postdoctoral Council.

References

1 C. Amatore and A. Jutand, *Acc. Chem. Res.*, 2000, **105**, 314–321.
2 S.-W. Kim, M. Kim, W. Y. Lee and T. Hyeon, *J. Am. Chem. Soc.*, 2002, **124**, 7642–7643.
3 R. Narayanan and M. A. El-Sayed, *J. Am. Chem. Soc.*, 2003, **125**, 8340–8347.

4 L. Aschwanden, T. Mallat, F. Krumeich and A. J. Baiker, *J. Mol. Catal. A: Chem.*, 2009, **309**, 57–62.
5 B. S. Takale, M. Bao and Y. Yamamoto, *Org. Biomol. Chem.*, 2014, **12**, 2005–2027.
6 C. Deraedt., R. Ye, W. T. Ralston, F. D. Toste and G. A. Somorjai, *J. Am. Chem. Soc.*, 2017, **139**, 18084–18092.
7 A. R. Tao, S. Habas and P. Yang, *Small*, 2008, **4**, 310–325.
8 J. Chen, B. Lim, E. P. Lee and Y. Xia, *Nano Today*, 2009, **4**, 81–95.
9 D. Wang and Y. Li, *J. Adv. Mater.*, 2011, **23**, 1044–1060.
10 Z. Quan, Y. Wang and J. Fang, *Acc. Chem. Res.*, 2013, **46**, 191–202.
11 F. J. Zhu, J. M. Kim, K.-C. Tsao, J. L. Zhang and H. Yang, *Curr. Opin. Chem. Eng.*, 2015, **8**, 89–97.
12 S. Zhang, X. Zhang, G. Jiang, H. Zhu, S. Guo, D. Su, G. Lu and S. Sun, *J. Am. Chem. Soc.*, 2014, **136**, 7734–7739.
13 B. P. Chaplin, M. Reinhard, W. F. Schneider, C. Schüth, J. R. Shapley, T. J. Strathmann and C. J. Werth, *Environ. Sci. Technol.*, 2012, **46**, 3655–3670.
14 X. Qu, J. Brame, Q. Li and P. J. Alvarez, *Acc. Chem. Res.*, 2013, **46**, 834–843.
15 X. Yu, A. Shavel, X. An, Z. Luo, M. Ibáñez and A. Cabot, *J. Am. Chem. Soc.*, 2014, **136**, 9236–9239.
16 Y. Zhang, J. Ahn, J. Liu and D. Qin, *Chem. Mater.*, 2018, **30**, 2151–2159.
17 S. Nie and S. R. Emory, *Science*, 1997, **275**, 1102–1106.
18 A. M. Michaels, M. Nirmal and L. E. Brus, *J. Am. Chem. Soc.*, 1999, **121**, 9932–9939.
19 J. P. Camden, J. A. Dieringer, Y. Wang, D. J. Masiello, L. D. Marks, G. C. Schatz and R. P. Van Duyne, *J. Am. Chem. Soc.*, 2008, **130**, 12616–12617.
20 A. B. Zrimsek, N. Wong and R. P. Van Duyne, *J. Phys. Chem. C*, 2016, **120**, 5133–5142.
21 A. B. Zrimsek, N. Chiang, M. Mattei, S. Zaleski, M. McAnally, C. Chapman, A.-I. Henry, G. C. Schatz and R. P. Van Duyne, *Chem. Rev.*, 2017, **117**, 7583–7613.
22 A. J. Haes, C. L. Haynes, A. D. McFarland, G. C. Schatz, R. P. Van Duyne and S. Zou, *MRS Bull.*, 2005, **30**, 368–375.
23 K. A. Willets and R. P. Van Duyne, *Annu. Rev. Phys. Chem.*, 2007, **58**, 267–297.
24 J. P. Camden, J. A. Dieringer, J. Zhao and R. P. Van Duyne, *Acc. Chem. Res.*, 2008, **41**, 1653–1661.
25 P. K. Jain, X. Huang, I. H. El-Sayed and M. A. El-Sayed, *Acc. Chem. Res.*, 2008, **41**, 1578–1586.
26 M. Rycenga, C. M. Cobley, J. Zeng, W. Li, C. H. Moran, Q. Zhang, D. Qin and Y. Xia, *Chem. Rev.*, 2011, **111**, 3669–3712.
27 Y. Zhang, X. Gao and M. J. Weaver, *J. Phys. Chem.*, 1993, **97**, 8656–8663.
28 Z.-Q. Tian, B. Ren, J.-F. Li and Z.-L. Yang, *Chem. Commun.*, 2007, 3514–3534.
29 Z.-Q. Tian, B. Ren and D.-Y. Wu, *J. Phys. Chem. B*, 2002, **106**, 9463–9683.
30 J. M. McLellan, Y. Xiong, M. Hu and Y. Xia, *Chem. Phys. Lett.*, 2006, **417**, 230–234.
31 B. Ren, G.-K. Liu, X.-B. Lian, Z.-L. Yang and Z.-Q. Tian, *Anal. Bioanal. Chem.*, 2007, **388**, 29–45.
32 W. Xie, B. Walkenfort and S. Schlücker, *J. Am. Chem. Soc.*, 2013, **135**, 1657–1660.
33 S. Link, Z. L. Wang and M. A. El-Sayed, *J. Phys. Chem. B*, 1999, **103**, 3529–3533.
34 X. Xia, Y. Wang, A. Ruditskiy and Y. Xia, *Adv. Mater.*, 2013, **25**, 6313–6333.
35 R. G. Sanedrin, D. G. Georganopoulou, S. Park and C. A. Mirkin, *Adv. Mater.*, 2005, **17**, 1027–1031.
36 S. E. Habas, H. Lee, V. Radmilovic, G. A. Somorjai and P. Yang, *Nat. Mater.*, 2007, **6**, 692–697.
37 C. J. DeSantis, A. C. Sue, M. M. Bower and S. E. Skrabalak, *ACS Nano*, 2012, **6**, 2617–2628.
38 Y. Xia, K. D. Gilroy, H. C. Peng and X. Xia, *Angew. Chem., Int. Ed.*, 2017, **56**, 60–95.
39 Y. Xia, Y. Xiong, B. Lim and S. E. Skrabalak, *Angew. Chem., Int. Ed.*, 2009, **48**, 60–103.
40 M. Rycenga, C. M. Cobley, J. Zeng, W. Li, C. H. Moran, Q. Zhang, D. Qin and Y. Xia, *Chem. Rev.*, 2011, **111**, 3669–3712.
41 K. D. Gilroy, A. Ruditskiy, H.-C. Peng, D. Qin and Y. Xia, *Chem. Rev.*, 2016, **116**, 10414–10472.
42 Y. Wu, X. Sun, Y. Yang, J. Li, Y. Zhang and D. Qin, *Acc. Chem. Res.*, 2017, **50**, 1774–1784.
43 H. Liu, T. Liu, L. Zhang, L. Han, C. Gao and Y. Yin, *Adv. Funct. Mater.*, 2015, **25**, 5435–5443.
44 Y. Yang, J. Liu, Z. Fu and D. Qin, *J. Am. Chem. Soc.*, 2014, **136**, 8153–8156.
45 X. Sun, Y. Yang, Z. Zhang and D. Qin, *Chem. Mater.*, 2017, **29**, 4014–4021.
46 J. Zhang, S. A. Winget, Y. Wu, D. Su, X. Sun, Z. X. Xie and D. Qin, *ACS Nano*, 2016, **10**, 2607–2616.
47 J. Huang, Y. Zhu, M. Lin, Q. Wang, L. Zhao, Y. Yang, K. X. Yao and Y. Han, *J. Am. Chem. Soc.*, 2013, **135**, 8552–8561.
48 J. Li, J. Liu, Y. Yang and D. Qin, *J. Am. Chem. Soc.*, 2015, **137**, 7039–7042.
49 J. Li, Y. Wu, X. Sun, J. Liu, S. A. Winget and D. Qin, *ChemNanoMat*, 2016, **2**, 786–790.
50 Y. Wu, D. Su and D. Qin, *ChemNanoMat*, 2017, **3**, 245–251.
51 J. Zeng, C. Zhu, J. Tao, M. Jin, H. Zhang, Z.-Y. Li, Y. Zhu and Y. Xia, *Angew. Chem., Int. Ed.*, 2012, **51**, 2354–2358.
52 W. Xie, C. Herrmann, K. Kömpe, M. Haase and S. Schlücker, *J. Am. Chem. Soc.*, 2011, **133**, 19302–19305.
53 Y. F. Huang, D. Y. Wu, H. P. Zhu, L. B. Zhao, G. K. Liu, B. Ren and Z.-Q. Tian, *Phys. Chem. Chem. Phys.*, 2012, **14**, 8485–8497.
54 Q. Zhang, D. A. Blom and H. Wang, *Chem. Mater.*, 2014, **26**, 5131–5142.
55 H. Zhang, X.-G. Zhang, J. Wei, C. Wang, S. Chen, H.-L. Sun, Y.-H. Wang, B.-H. Chen, Z.-L. Yang, D.-Y. Wu, J.-F. Li and Z.-Q. Tian, *J. Am. Chem. Soc.*, 2017, **139**, 10339–10346.
56 J.-F. Li, Y.-J. Zhang, S.-Y. Ding, R. Panneerselvam and Z.-Q. Tian, *Chem. Rev.*, 2017, **117**, 5002–5069.

